Chinese Chemical Letters 37 (2026) 112126

Contents lists available at ScienceDirect

Chinese Chemical Letters

journal homepage: www.elsevier.com/locate/cclet

Mitochondria-targeted and magnetic resonance imaging of water-stable trilobate-shaped nonanuclear lanthanide clusters

Meng-Juan Tang[a], Zhong-Hong Zhu[b], Hai-Ling Wang[b,*], Fu-Pei Liang[a], Hua-Hong Zou[a,*]

[a] Key Laboratory for Chemistry and Molecular Engineering of Medicinal Resources (Ministry of Education of China), Guangxi Key Laboratory of Chemistry and Molecular Engineering of Medicinal Resources, School of Chemistry and Pharmaceutical Sciences, Guangxi Normal University, Guilin 541004, China
[b] School of Chemistry and Chemical Engineering, Guangxi Key Laboratory of Electrochemical Energy Materials, Guangxi University, Nanning 530004, China

ARTICLE INFO

Article history:
Received 6 July 2025
Revised 4 November 2025
Accepted 16 November 2025
Available online 17 November 2025

Keywords:
Lanthanide clusters
Solvothermal synthesis
Luminescence
Cell imaging
Magnetic resonance imaging

ABSTRACT

The construction of lanthanide nanoclusters that are stable in aqueous solution is challenging, which has led to a sluggish application in the field of bioimaging. Herein, a chelating ligand protection strategy was used to construct nonanuclear lanthanide clusters (**Ln$_9$**, Ln = Eu, Dy, and Gd) that is stable in aqueous solution. The first fluorescence imaging performance of lanthanide clusters targeting mitochondrial organelles was achieved, with colocalization coefficients of up to 0.96 (MCF-7) and 0.93 (MDA-MB-231) with commercial mitochondrial dyes, respectively. **Eu$_9$** can be rapidly taken up by zebrafish and shows excellent fluorescence imaging results, demonstrating its excellent *in vivo* imaging performance. In addition, the longitudinal and transverse relaxation rates r_1 and r_2 of **Gd$_9$** with highly aggregated Gd(III) ions are 39.42 and 50.58 mmol L^{-1} s^{-1}, respectively, showing great application potential as a new and efficient T_1-weighted nanocluster-based magnetic resonance imaging contrast agents.

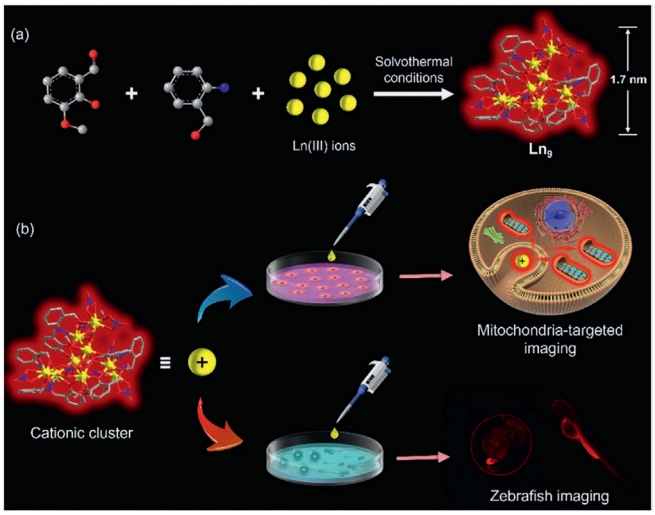
© 2026 Published by Elsevier B.V. on behalf of Chinese Chemical Society and Institute of Materia Medica, Chinese Academy of Medical Sciences.

As a molecular aggregate with precise structural information and unique electronic characteristics, lanthanide nanoclusters have become a bridge between microscopic molecules and macroscopic nanoparticles, and occupy an irreplaceable position in the fields of synthetic chemistry and material chemistry [1–5]. Compared with other nanomaterials, lanthanide nanoclusters have a strictly defined composition and geometric configuration, allowing their photophysical properties to establish a clear correlation with the structure, thus providing a solid foundation for the study of imaging mechanisms. Through ideas such as ligand design, core number regulation and assembly strategy optimization, a series of lanthanide nanoclusters with high symmetry, multi-core structure and precise coordination environment have been successfully constructed [6–11]. Thanks to the special configuration of the 4*f* electron layer, the lanthanide nanoclusters have shown excellent photoelectromagnetic properties and have made significant progress in the fields of ultra-low temperature magnetic refrigeration and solid-state luminescence [12–15]. However, compared with the widespread application of the solid-state field, the application expansion of lanthanide nanoclusters in solutions is relatively lagging, mainly because they face a series of problems such as poor stability, poor dispersion and luminescence quenching in solutions [16–18].

In recent years, our research team has proposed a multidentate chelate coordination (MCC) for directed construction of stable lanthanide nanoclusters in solution [19,20]. Based on the MCC, a series of stable lanthanide nanoclusters have been obtained and their optical imaging and sensing properties in aqueous solutions have been expanded [21–23]. In 2024, our team used the MCC to synthesize a case of **Eu$_9$Zn$_8$** nanocluster with dual antenna effects and achieved high-resolution cell imaging effects [22]. In 2025, we used polyoxygenate **Mo$_8$** as an antenna to synthesize luminescent **EuMo$_{16}$**, achieving specific antibiotic-enhanced antenna effect behavior [23]. Contrast agents (CAs) are substances that can significantly enhance image contrast by altering the physical or chemical properties of tissues or organs. Clinically, Gd(III) chelates are the most common CAs for nuclear magnetic resonance imaging (MRI) [24,25]. So far, the relaxation rate of these Gd(III) chelates is low, and the need for high doses has caused a series of problems such as nephrotoxicity [26]. According to the Solomon-Bloembergen-Morgan (SBM) relaxation theory, multi-core Gd(III) clusters constructed using multi-component integration strategy can significantly improve relaxation efficiency, thereby effectively reducing the risk of CAs in clinical applications [27]. At present, the construction of lanthanide nanoclusters with both MRI and optical imaging functions is still in its infancy [28,29].

* Corresponding authors.
E-mail addresses: whl2016010984@163.com (H.-L. Wang), gxnuchem@foxmail.com (H.-H. Zou).

https://doi.org/10.1016/j.cclet.2025.112126
1001-8417/© 2026 Published by Elsevier B.V. on behalf of Chinese Chemical Society and Institute of Materia Medica, Chinese Academy of Medical Sciences.



Scheme 1. Schematic diagram of the synthesis, mitochondrial imaging and *in vivo* imaging of **Eu$_9$** nanocluster.

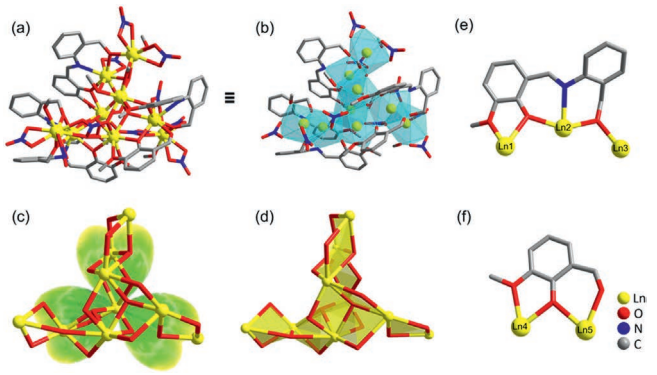


Fig. 1. (a, b) Structural of **Ln$_9$** clusters. (c, d) Schematic representation of the metal cluster nucleus. Coordination patterns of ligands $(L^1)^{2-}$ (e) and $(L^2)^-$ (f).

Obviously, the expansion of lanthanide nanoclusters with both MRI and optical imaging functions provides new imaging methods for early diagnosis of diseases.

Herein, three yellow block crystals were obtained by reacting 2-aminobenzyl alcohol, *o*-vanillin and $Ln(NO_3)_3{\cdot}6H_2O$ (Ln = Eu, Dy, and Gd) under solvent thermal conditions, and their molecular formulas were $[Ln_9(L^1)_4(L^2)(NO_3)_{10}(CH_3O)(\mu_2\text{–}OH)_2(\mu_3\text{–}OH)_3(CH_3OH)_5](NO_3)_2{\cdot}xCH_3OH{\cdot}yCH_3CN$ (Ln = Eu, $x = 7$, $y = 9$; Dy, $x = 7$, $y = 4$; Gd, $x = 7$, $y = 9$; H_2L^1 = 2–methoxy-6-[(*E*)-2′-hydroxymethyl-phenyliminomethyl]phenol; HL^2 = *o*-vanillin). High resolution electrospray mass spectrometry (HRESI-MS) results prove that nanocluster **Ln$_9$** has high stability in solution. In addition, time-dependent HRESI-MS tracks the formation process of **Dy$_9$** clusters, identifying changes in multiple intermediates, and revealing that it may be formed through a multi-template assembly mechanism. It is worth noting that the lanthanide nanocluster **Eu$_9$**, which is low in biotoxicity, uniform in size and positive charge, can still achieve excellent imaging effects under low concentration incubation, and exhibit excellent mitochondrial targeting capabilities in both MDA-MB-231 and MCF-7 cells (Scheme 1). To the best of our knowledge, this is the first application of lanthanide nanoclusters for mitochondria-specific fluorescence imaging, and this finding provides an important reference for the development of novel lanthanide nanoclusters for subcellular organelle localization. In addition, in zebrafish and its embryo models, **Eu$_9$** also showed selective marking ability to the egg envelope, yolk sac and digestive system. The low concentration of **Gd$_9$** has a high relaxation rate ($r_1 = 39.42$ mmol L^{-1} s^{-1}, and $r_2 = 50.58$ mmol L^{-1} s^{-1}) at a magnetic field intensity of 0.5 T, indicating its excellent MRI application potential. **Ln$_9$** offers new insights into developing lanthanide nanoclusters with potential for high-resolution imaging applications.

Single crystal X-ray diffraction (SCXRD) indicates that nonanuclear **Ln$_9$** crystallizes in the *P*-1 space group of the triclinic crystal system (Tables S1 and S2 in Supporting information). **Ln$_9$** consists of 9 Ln(III) ions, 4 ligands $(L^1)^{2-}$ that remove two protons, 1 ligand $(L^2)^-$ that removes one proton, 10 NO_3^-, 1 CH_3O^-, 5 OH^-, 5 CH_3OH, and peripheral guest molecules. Their molecular formulas are $[Ln_9(L^1)_4(L^2)(NO_3)_{10}(CH_3O)(\mu_2\text{–}OH)_2(\mu_3\text{–}OH)_3(CH_3OH)_5](NO_3)_2{\cdot}xCH_3OH{\cdot}yCH_3CN$ (Ln = Eu, $x = 7$, $y = 9$; Dy, $x = 7$, $y = 4$; Gd, $x = 7$, $y = 9$; H_2L^1 = 2–methoxy-6-[(*E*)-2′–hydroxy methyl-phenyliminomethyl]-phenol; HL^2 = *o*-vanillin) (Figs. 1a and b). The nonanuclear **Ln$_9$** cluster core can be viewed as a triangular framework that extends in three different directions, generating a binuclear structure. Generally, due to the unique spatial extension mode of electrons and the high coordination number of Ln^{3+} ions, the nonanuclear lanthanide clusters tend to form highly symmetric "hourglass-type" cluster nuclei [30–32]. The lowest energy effect brought by high symmetry gives "hourglass" clusters an absolute advantage in solution self-assembly and crystal stacking. However, the structural characteristics of nonanuclear **Ln$_9$** clearly deviate from this common pattern: the cluster core of **Ln$_9$** can be abstracted into a triangular frame, in which three vertices are occupied by an 8-coordinated and two 9-coordinated Ln^{3+}, and the three sides extend outward from the dual-core unit, forming three radial arms. This structural feature forms a sharp contrast with the "hourglass" cluster core. The difference between nonanuclear lanthanide clusters **Ln$_9$** and the highly symmetric "hourglass" cluster provides new topological sites for solvent molecules, counter ions and guest molecules, enriching the structural database of lanthanide metal complexes. The {Dy/O} cluster nucleus of nonanuclear **Ln$_9$** is formed by the oxygen atoms on the deprotonated ligand, OH^- and NO_3^- bridging the nine Ln(III) ions through the co-formation (Figs. 1c and d). The $(L^1)^{2-}$ ligand within the nonanuclear **Ln$_9$** structure chelates three Ln(III) ions, with a coordination mode of $\mu_3\text{-}\eta^2\text{:}\eta^1\text{:}\eta^2\text{:}\eta^1$ (Fig. 1e). In addition, the $(L^2)^-$ ligand chelates two Ln (III) ions separately, with a coordination mode of $\mu_2\text{-}\eta^1\text{:}\eta^2\text{:}\eta^1$ (Fig. 1f). The nine Ln(III) ions within the nonanuclear **Ln$_9$** structure possess five different coordination environments, indicating its relatively low symmetry (Tables S3-S7 in Supporting information) [33]. The thermogravimetric analysis test proved that the number of free guest molecules outside the nonanuclear **Ln$_9$** structure was consistent with the molecular formula (Fig. S2 in Supporting information). The absorption peaks of the Fourier transform infrared (FT-IR) absorption spectrum of nonanuclear **Ln$_9$** were located at 1460, 1384, 1295, 1231, and 738 cm^{-1}, respectively, which can be attributed to the bending vibration of the C–H bond, symmetric deformation vibration of -CH_3, out-of-plane bending vibration of the C–H bond of the benzene ring, the stretching vibration of the C–O bond, and the out-of-plane bending vibration (Fig. S3a in Supporting information). The observed and simulated values of powder X-ray diffraction (PXRD) of nonanuclear **Ln$_9$** at ambient temperature and pressure are in high agreement, proving that they are all pure phases (Fig. S3b in Supporting information). Scanning electron microscopy (SEM) also verified the cleanliness of the nonanuclear **Dy$_9$** surface (Fig. S4 in Supporting information).

A small amount of **Dy$_9$** crystals was dissolved in chromatographically pure acetonitrile and subsequently diluted extensively with chromatographically pure anhydrous methanol for high-resolution electrospray mass spectrometry (HRESI-MS) test-

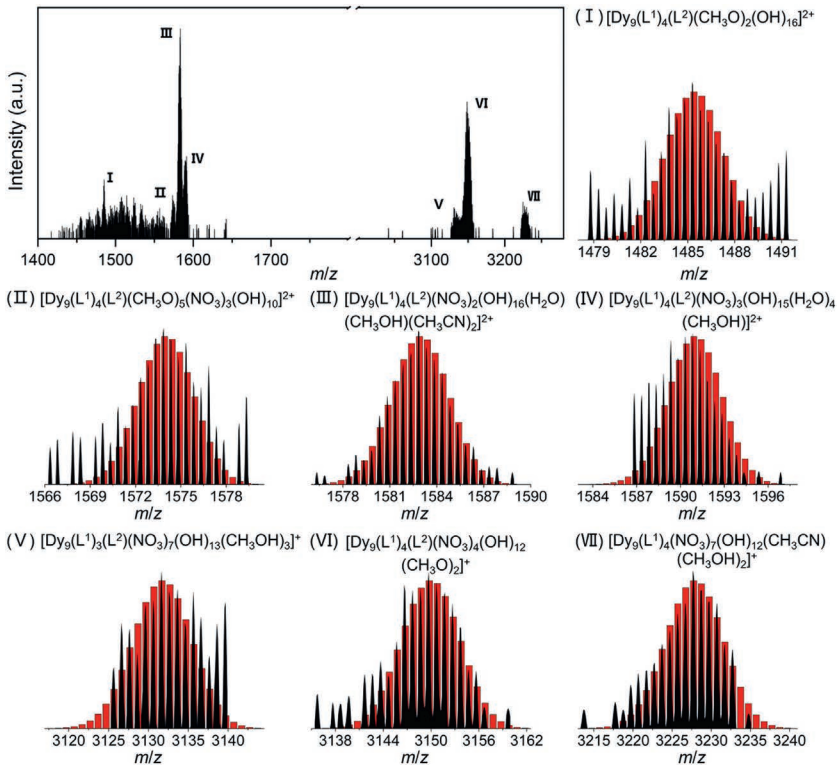


Fig. 2. HRESI-MS spectrum of **Dy_9** in positive ion mode.

ing [16,19]. HRESI-MS analysis showed that molecular ion peaks highly consistent with the nonanuclear **Dy_9** body frame were detected, indicating that **Dy_9** exhibited high stability in the above solutions. As shown in Fig. 2, the molecular ion peaks of HRESI-MS of **Dy_9** cluster were attributed and fitted as follows: $[Dy_9(L^1)_4(L^2)(CH_3O)_2(OH)_{16}]^{2+}$ (Cal. 1485.32, Exp. 1485.40), $[Dy_9(L^1)_4(L^2)(CH_3O)_5(NO_3)_3(OH)_{10}]^{2+}$ (Cal. 1573.85, Exp. 1573.92), $[Dy_9(L^1)_4(L^2)(NO_3)_2(OH)_{16}(H_2O)(CH_3OH)(CH_3CN)_2]^{2+}$ (Cal. 1582.34, Exp. 1582.44), $[Dy_9(L^1)_4(L^2)(NO_3)_3(OH)_{15}(H_2O)_4(CH_3OH)]^{2+}$ (Cal. 1590.85, Exp. 1590.92), $[Dy_9(L^1)_3(L^2)(NO_3)_7(OH)_{13}(CH_3OH)_3]^{+}$ (Cal. 3131.67, Exp. 3131.70), $[Dy_9(L^1)_4(L^2)(NO_3)_4(OH)_{12}(CH_3O)_2]^{+}$ (Cal. 3149.68, Exp. 3149.78), $[Dy_9(L^1)_4(NO_3)_7(OH)_{12}(CH_3CN)(CH_3OH)_2]^{+}$ (Cal. 3227.69, Exp. 3227.75). Combined with structural analysis, the peripheral ligands $(L^1)^{2-}$, $(L^2)^{-}$ and NO_3^{-} all form a tight protective shell for the cluster nuclei of nonanuclear **Ln_9** clusters, enhancing the ability of the clusters to withstand attack by external guest molecules (Fig. S5 in Supporting information). Clearly, this structural feature provides a foundation for exploring the assembly mechanisms and potential applications of such lanthanide clusters in solution.

Time-dependent HRESI-MS was utilized to monitor changes in species at different time points during **Dy_9** formation. The resolution and intensity changes of the molecular ion peaks were utilized to speculate on the possible assembly mechanism of **Dy_9**. As shown in Fig. 3, molecular ion peaks were collected at multiple time points (*i.e.*, 0, 30 min and 1, 2, 3, 6, 12, 24, 48 h) in the $m/z = 200 \sim 4000$ range, and 13 relevant molecular ion peaks were monitored. At the start of the reaction (at 0 min), the molecular ion peak of the organic ligand HL^2 was monitored ($m/z = 266.25$). As the reaction progresses, the signal intensity associated with the HL^2 ligand peaks and then decreases in intensity. This phenomenon suggests that the HL^2 ligand is involved in coordination in the reaction system and subsequently in the assembly process. The above debris can be attributed: $[(C_8H_8O_3)(CH_3CN)(H_2O)_4]^{+}$ (Cal. 266.25, Exp. 266.12) (Fig. S6a in Supporting information).

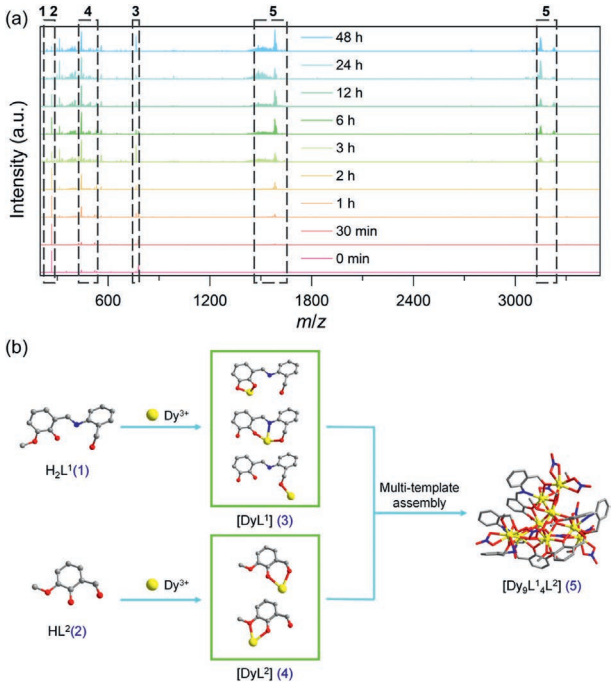


Fig. 3. (a) Time-dependent HRESI-MS spectrum of **Dy_9** in the range of $m/z = 200 \sim 4000$. (b) Schematic diagram of possible assembly mechanism of **Dy_9**.

As the reaction progressed to 2 h, molecular ion peaks associated with the organic ligand H_2L^1 began to be detected, with fragments attributed to the $(C_{15}H_{15}NO_3)^{+}$ (Cal. 258.12, Exp. 258.11) (Fig. S6b in Supporting information). However, at the beginning of the reaction initiation (0 min), a fragmentation peak of DyL^1 was already detected, indicating that the organic ligand H_2L^1 rapidly

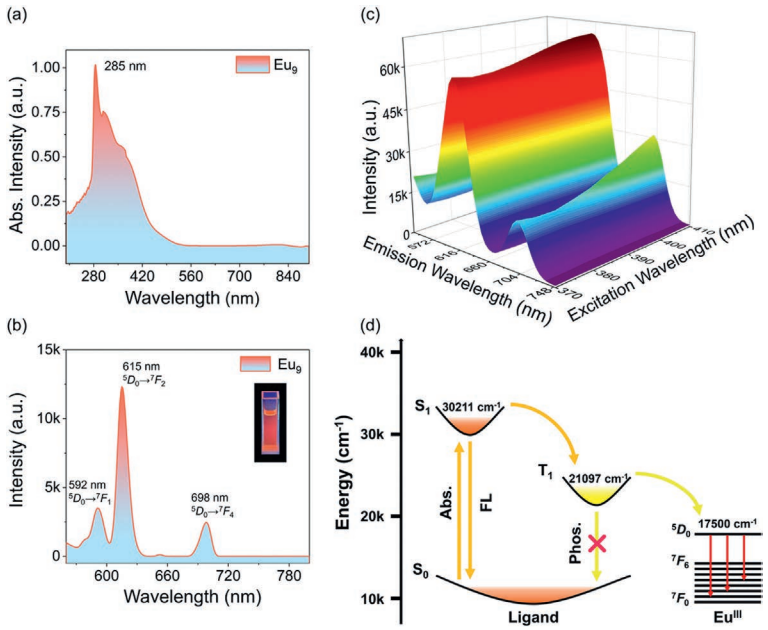


Fig. 4. (a) UV–vis absorption spectrum of **Eu$_9$**. (b) Emission spectrum of **Eu$_9$** solution. (c) Excitation wavelength-dependent emission spectrum of **Eu$_9$**. (d) Energy transfer pathway and antenna effect of **Eu$_9$** analyzed using *Jablonsky* energy level diagram.

coordinated with the Dy(III) ion to form a fragment of DyL^1. Therefore, the molecular ion peak associated with H_2L^1 was not observed at the onset of the reaction. The intensity of the DyL^1 fragment peaked at 3 h and diminished with reaction time. These molecular ion peaks are attributed to $[Dy(L^1)(CH_3O)(CH_3CN)_2]^+$ (Cal. 532.99, Exp. 533.10), $[Dy(L^1)(NO_3)(CH_3CN)_3(CH_3OH)(H_2O)_8]^+$ (Cal. 780.26, Exp. 780.20) (Fig. S7 in Supporting information). In the range of $m/z = 426.95 \sim 521.95$, three molecular ion peaks associated with DyL^2 fragments were detected, which were formed by chelating Dy(III) ions with the organic ligand HL^2. The molecular ion peak of DyL^2 can correspond to the following species: $[Dy(L^2)(NO_3)_2(CH_3CN)_2]^+$ (Cal. 521.95, Exp. 522.00), $[Dy(L^2)(NO_3)(OH)(CH_3OH)(H_2O)]^+$ (Cal. 443.94, Exp. 444.00), $[Dy(L^2)(NO_3)(OH)(CH_3OH)]^+$ (Cal. 426.95, Exp. 426.99) (Fig. S8 in Supporting information). Finally, six major backbone peaks of $[Dy_9(L^1)_4(L^2)]$ were detected in the interval of $m/z = 1485.32 \sim 3227.69$. These characteristic fragments were first observed at 1 h and as the reaction progressed, their number intensity gradually increased and reached a peak at 48 h. Attribution of these molecular ion peaks: $[Dy_9(L^1)_4(L^2)(CH_3O)_2(OH)_{16}]^{2+}$ (Cal. 1485.32, Exp. 1485.40), $[Dy_9(L^1)_4(L^2)(CH_3O)_5(NO_3)_3(OH)_{10}]^{2+}$ (Cal. 1573.85, Exp. 1573.92), $[Dy_9(L^1)_4(L^2)(NO_3)_2(OH)_{16}(H_2O)(CH_3OH)(CH_3CN)_2]^{2+}$ (Cal. 1582.34, Exp. 1582.44), $[Dy_9(L^1)_4(L^2)(NO_3)_3(OH)_{15}(H_2O)_4(CH_3OH)]^{2+}$ (Cal. 1590.85, Exp. 1590.92), $[Dy_9(L^1)_3(L^2)(NO_3)_7(OH)_{13}(CH_3OH)_3]^+$ (Cal. 3131.67, Exp. 3131.70), $[Dy_9(L^1)_4(L^2)(NO_3)_4(OH)_{12}(CH_3O)_2]^+$ (Cal. 3149.68, Exp. 3149.78), $[Dy_9(L^1)_4(NO_3)_7(OH)_{12}(CH_3CN)(CH_3OH)_2]^+$ (Cal. 3227.69, Exp. 3227.75). HRESI-MS results show that the $[DyL^1]$ template primitive and the $[DyL^2]$ template primitive may be assembled through a multi-template assembly mechanism to form the final cluster $[Dy_9(L^1)_4(L^2)]$.

Exploration of the optical properties of metal complexes is crucial for their application in high-resolution imaging [34]. Under irradiation of 365 nm ultraviolet lamps, the bright red luminescence of **Eu$_9$** solution was observed, proving its potential application value in the field of optical. The UV–visible (UV–vis) absorption spectrum of **Eu$_9$** showed a wide absorption peak at 280-430 nm (Fig. 4a). In addition, under 365 nm excitation, **Eu$_9$** showed obvious characteristic emission peaks of Eu(III) ions at 592, 615 and 698 nm, respectively, which can be attributed to the characteristic energy level transitions of $^5D_0 \rightarrow {}^7F_1$, $^5D_0 \rightarrow {}^7F_2$ and $^5D_0 \rightarrow {}^7F_4$ of Eu(III) ions, respectively (Fig. 4b). As shown in Fig. 4c, within the range of the excitation wavelength gradually increased from 370 nm to 410 nm, **Eu$_9$** clearly showed the characteristic emission of Eu(III) ions. The above results show that ligands around the **Eu$_9$** cluster can act as efficient antennas and sensitize the emission of Eu(III) ions through antenna effects.

To understand the energy transfer pathway of **Eu$_9$**, a *Jablonsky* energy level diagram was drawn (Fig. 4d). Following Reinhoudt's empirical guidelines, the inter-system crossing (ISC) process will be efficient when the energy level difference between the lowest singlet excited state (S_1) and the lowest excited triplet state (T_1) of the ligand reaches or exceeds 5000 cm^{-1} [35–37]. Based on the solid-state UV–vis absorption spectroscopy data of H_2L^1, the energy level of S_1 is 30,211 cm^{-1} (Fig. S9 in Supporting information). We obtained the solid phosphorescence spectrum of **Gd$_9$** at 77 K and performed Gaussian curve fitting to derive the T_1 energy value for H_2L^1, which was 21,097 cm^{-1} (Fig. S10 in Supporting information). Therefore, the energy difference (ΔE_1) between S_1 and T_1 of H_2L^1 is 9114 cm^{-1}. Obviously, the above ΔE is significantly greater than 5000 cm^{-1}, confirming that there is an efficient ISC process between the S_1 and T_1 energy levels of H_2L^1. According to Latva's rule of thumb, the optimal energy level difference (ΔE) between the $^5D_0$ energy level of Eu(III) ions and T_1 capable of efficient energy transfer processes is 2000~5000 cm^{-1} [38,39]. The energy level of the $^5D_0$ energy level of Eu(III) ion is 17,500 cm^{-1}. Obviously, the ΔE between the T_1 energy level of H_2L^1 and the $^5D_0$ energy level of Eu(III) ion is 3597 cm^{-1}, proving that H_2L^1 can emit light as a characteristic of efficient antenna-sensitized Eu(III) ion.

Compared with single-metal or low-core lanthanide complexes, high-nuclear lanthanide clusters not only have the quantum size effect brought by nanosize, but also highly concentrated metal centers within the clusters can often promote the development of new functions. Dynamic light scattering (DLS) results indicate that **Eu$_9$**, **Dy$_9$**, and **Gd$_9$** clusters form uniformly dispersed nanoparticles in aqueous solution, with hydrated diameters of 118.2, 88.89, and 111.37 nm, respectively (Fig. 5a and Fig. S11 in Supporting

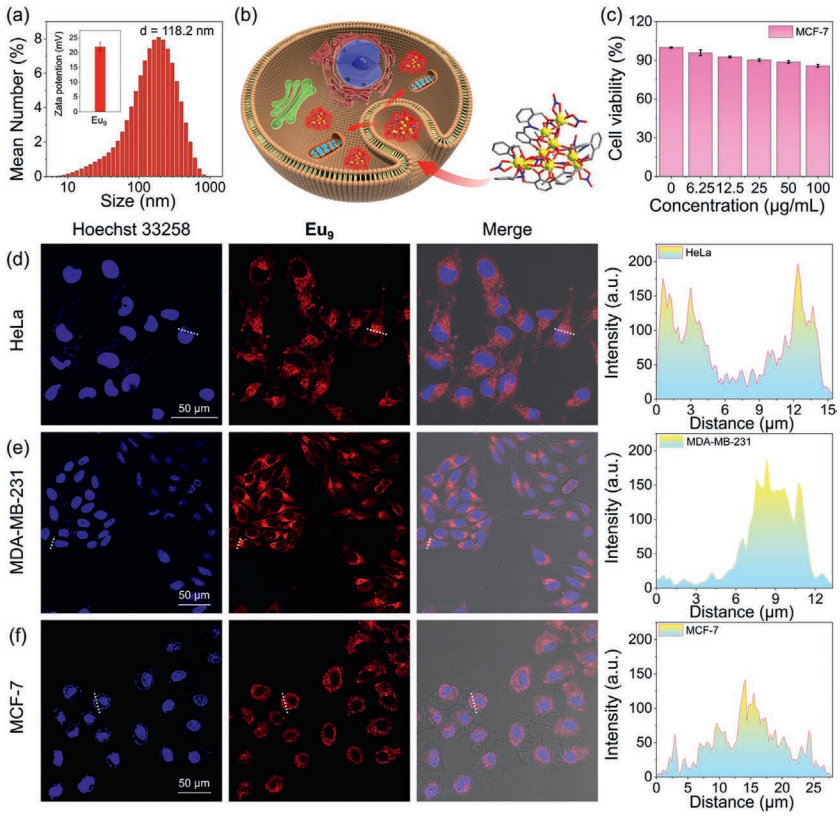


Fig. 5. (a) Size distribution and zeta potential of nanocluster **Eu$_9$** dispersed in water. (b) Schematic diagram of cell imaging of **Eu$_9$**. (c) Concentration-dependent growth inhibition rate of **Eu$_9$** on MCF-7 cells; CLSM images and quantitative analysis of fluorescence intensity after co-incubation with HeLa (d), MDA-MB-231 (e) and MCF-7 (f) cells, respectively.

information). The stability of **Eu$_9$** and **Gd$_9$** in physiological media was confirmed by dispersing them in PBS, complete RPMI-1640, and Dulbecco's Modified Eagle Medium. Over five days, their UV–vis absorbance at 406 nm exhibited negligible variation, exhibiting excellent stability under biologically relevant conditions (Fig. S12 in Supporting information). Furthermore, as shown in Fig. 5a, the zeta potential of the **Eu$_9$** cluster in the aqueous solution was 22 mV, confirming that its nanoparticles have high stability in the aqueous solution. The potential toxicity of concentration-dependent **Eu$_9$** solutions (0, 6.25, 12.5, 25, 50, 100 μg/mL) to different cells was evaluated using 3-(4,5-dimethylthiazole-2-yl)-2,5-diphenyltetraazole bromine salt (MTT). As shown in Fig. 5c and Fig. S13 (Supporting information), after incubating HeLa, MDA-MB-231, HepG2, 4T1, SK-OV-3, MCF-7 and WI-38 cells with concentration-dependent **Eu$_9$** solutions for 16 h, the cell survival rate exceeded 75%, demonstrating that **Eu$_9$** has low cytotoxicity. The performance of **Eu$_9$** in the optical imaging field of HeLa, MDA-MB-231, HepG2, 4T1, SK-OV-3, MCF-7 and WI-38 cells was further explored. Cells incubated in **Eu$_9$**/DMEM solution at a concentration of 25 μg/mL for 16 h were analyzed by *in vitro* cell imaging using two-photon confocal laser scanning microscopy (CLSM). The results show that the **Eu$_9$** cluster can be effectively uptaken by a variety of different cells (Figs. 5d-f, Figs. S14 and S15 in Supporting information). Quantitative analysis of single-cell fluorescence intensity showed that the fluorescence intensity of **Eu$_9$** showed a decreasing trend in cells from HeLa to WI-38, and the specific fluorescence intensity was ranked as HeLa > MDA-MB-231 > MCF-7 > SKOV3 > 4T1 > HepG2 > WI-38. Obviously, different cells have differentiated uptake capabilities for **Eu$_9$** nanoclusters, and the **Eu$_9$** nanoclusters have high-resolution optical imaging effects on multiple cells, indicating the application potential of lanthanide nanoclusters in early cancer diagnosis.

Mitochondria play a central role in cellular metabolism, serving not only as key sites for energy conversion but also participating in the regulation of apoptosis, signal transduction, metabolic homeostasis, and immune defense [40,41]. These functions make mitochondria key to studying cellular function and disease mechanisms. To explore the precise positioning of **Eu$_9$** cluster for specific organelles in cells, commercial mitochondrial green fluorescent probes (Mito-Tracker Green) and lysosomal green fluorescent probes (Lyso Tracker Green) were used for colocalization experiments with **Eu$_9$** cluster (Fig. 6, Figs. S16 and S17 in Supporting information). The experimental results show that the **Eu$_9$** cluster and Mito-Tracker Green show bright red and green fluorescence in the red and green channels, respectively, and the fluorescence signals of the two show extremely high overlap. The correlation of fluorescence intensity of these two channels was quantified by colocalization coefficient, which was as high as 0.96 in MCF-7 cells (Fig. 6c) and 0.93 in MDA-MB-231 cells (Fig. 6d), indicating that there is a strong correlation between the **Eu$_9$** cluster and Mito-Tracker Green (Figs. S17 and S18 in Supporting information). At the same time, we also studied the colocalization imaging experiment of **Eu$_9$** in murine-derived cell 4T1. As shown in Fig. S18, the co-localization coefficient of **Eu$_9$** clusters and Mito-Tracker Green in 4T1 cells was 0.87. In addition, comparative experiments were performed on HeLa cells using **Eu$_9$** cluster and Lyso Tracker Green. Experimental results show that there is only a small overlap area between the red fluorescence generated by the **Eu$_9$** cluster and the green fluorescence generated by Lyso Tracker Green. The calculated colocation coefficient is only 0.4 (Fig. S17). The above experimental results show that the **Eu$_9$** cluster has excellent mitochondrial localization ability and can specifically label mitochondria in cells. In general, mitochondria-specific fluorescent labeled dyes are designed based on the positive electrical properties of

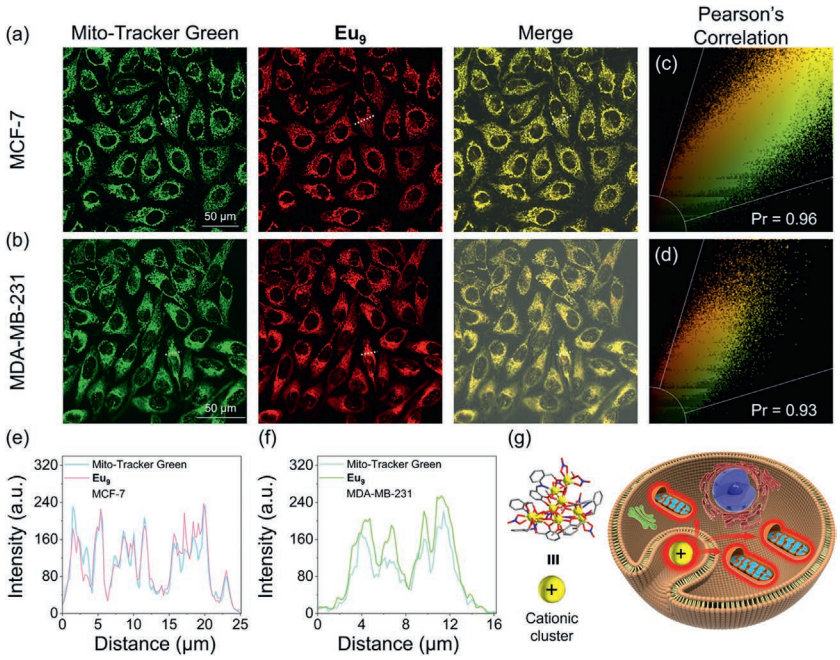


Fig. 6. CLSM images and colocalization coefficients of **Eu$_9$** and Mito-Tracker Green after 16 h of incubation in MCF-7 (a, c) and MDA-MB-231 (b, d). The fluorescence intensities of **Eu$_9$** and Mito-Tracker Green in MCF-7 (e) and MDA-MB-231 (f) cells were quantitatively analyzed. (g) Schematic diagram of mitochondrial imaging of **Eu$_9$**.

cationized molecules such as pyridine derivatives and quaternary ammonium salts. As a new cationic luminescent material—cationic cluster, cluster **Eu$_9$** can be attracted by the mitochondrial membrane potential due to its positive charge characteristics and then gather in the mitochondria. To our knowledge, this is the first time that specific fluorescent labeling application of lanthanide cluster mitochondrial organelles has been realized. This discovery not only enriches the scope of mitochondria-specific fluorescent probes, but also opens a door for the application of lanthanide nanoclusters in suborganelle imaging.

In the field of biomedical science, choosing the right biological model is crucial for biological imaging, disease mechanism exploration, drug response research, and therapeutic method development. Zebrafish and their embryos have significant advantages in biomedical research, which are mainly reflected in the following aspects: highly similar biological characteristics to humans, transparent embryos for easy observation, suitable for high-throughput experiments, and low research costs [42,43]. These advantages make zebrafish an ideal model for studying human disease and drug response. Here, we exposed fertilized zebrafish embryos to 25 μg/mL of **Eu$_9$** and incubated for 1, 2, 3, 6 and 12 h, respectively, to evaluate the imaging ability and distribution characteristics of **Eu$_9$** in zebrafish embryos. As shown in Fig. 7a, after fertilized zebrafish embryos, after 3 h incubation with **Eu$_9$**, a slight red fluorescence accumulation occurred in the egg envelope and yolk sac areas, indicating that **Eu$_9$** has the ability to enter the embryo through the chorionic. As the incubation time is extended, the fluorescence intensity gradually increases and the fluorescence distribution range is also expanded accordingly, which indicates that the increase of **Eu$_9$** entering the embryo (Fig. 7a and Fig. S19 in Supporting information). The significant difference in fluorescence intensity of the egg envelope, yolk sac and intraembryonic region revealed that **Eu$_9$** has selective affinity for different tissues inside the embryo.

Immediately afterwards, newly hatched zebrafish were exposed to 25 μg/mL of **Eu$_9$** and incubated for 1, 2, 3, 6 and 12 h, respectively, to evaluate the imaging ability and distribution characteristics of **Eu$_9$** in zebrafish [44]. Fig. 7b shows that newly hatched

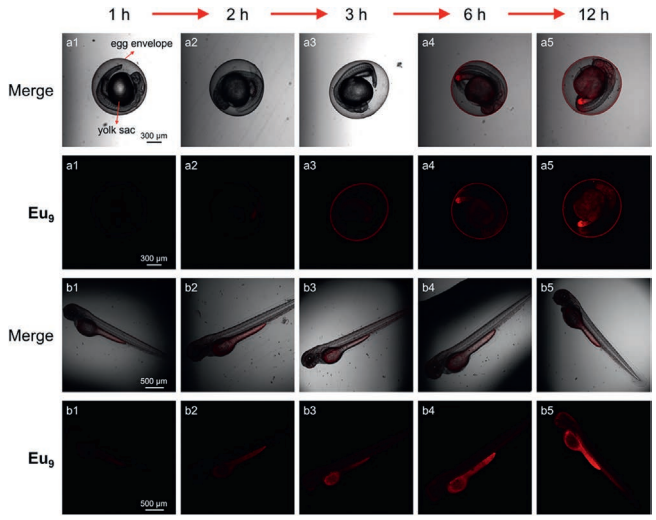


Fig. 7. Fluorescence images of **Eu$_9$** at a concentration of 25 μg/mL after co-incubation with zebrafish embryos (a) and juveniles (b) for 1, 2, 3, 6 and 12 h, respectively.

zebrafish exhibited a slight red fluorescence aggregation after 2 h of incubation with **Eu$_9$**, mainly concentrated in the digestive system and yolk sac region of the zebrafish. This phenomenon shows that **Eu$_9$** can enter zebrafish through swallowing and skin absorption mechanisms. At the same time, similar to the zebrafish embryo imaging phenomenon, zebrafish also showed that with the increase in incubation time, the fluorescence intensity *in vivo* gradually increased, and the fluorescence distribution range expanded accordingly (Fig. 7b). When the incubation time reached 12 h, the zebrafish head showed a faint red fluorescence signal. This may be caused by the fact that **Eu$_9$** is transported to the head area through blood circulation and other channels after being absorbed by the digestive system. The above experimental results show that **Eu$_9$** can efficiently enter zebrafish and its embryos and show op-

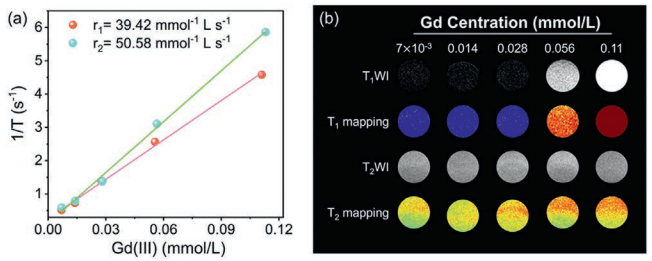


Fig. 8. (a) Comparison of imaging of solutions with different **Gd_9** concentrations in a 0.5 T magnetic field. (b) Comparison of r_1 and r_2 of **Gd_9** in a 0.5 T magnetic field.

tical imaging effects specific to specific tissues. At present, there are still few cases of applying lanthanide nanoclusters to the field of zebrafish imaging. This work not only develops excellent optical imaging probes based on lanthanide nanoclusters, but also opens new horizons for the biomedical application of lanthanide nanoclusters.

Magnetic resonance imaging (MRI) plays an important role in clinical medical diagnosis as a mature medical imaging technology. However, because of the problem of insufficient contrast in some cases, it is often necessary to enhance the imaging effect by using CAs. Therefore, it is necessary to design and develop CAs with high resolution and clear imaging effects [45–47]. T_1-weighted MRI CAs, which are now widely used as clinical diagnostics, are gadolinium-based chelates, and their superior imaging is dependent on higher doses. To explore the feasibility of **Gd_9** as a T_1-weighted MRI CA, we tested the relaxation time with the Gd(III) concentration changes at 0.5 T magnetic field strength and obtained the longitudinal and transverse relaxation rates (r_1 and r_2, respectively) (Fig. 8). The results show that the values of r_1 and r_2 values of **Gd_9** are 39.42 and 50.58 mmol L^{-1} s^{-1}, respectively, at 0.5 T magnetic field. **Gd_9** with a highly aggregated Gd(III) exhibited higher relaxation rates compared to the conventional Gd chelates (Fig. 8a). $r_2/r_1 = 1.28$ ($r_2/r_1 < 2$) indicated that **Gd_9** is a potential T_1-weighted MRI CA candidate. With the gradual increase of the Gd(III) concentration of **Gd_9** in the aqueous solution, the T_1-weighted image gradually became brighter under 0.5 T magnetic field (Fig. 8b). In contrast, the change in T_2-weighted images was not significant, indicating that **Gd_9** exhibits good T_1 imaging in solution. The T_1 mapping images displayed by different **Gd_9** concentrations at 0.5 T magnetic field also depicted its great potential as an MRI CA in biomedical diagnosis. Furthermore, we used the MTT method to evaluate the potential toxicity of concentration-dependent **Gd_9** solutions (0, 6.25, 12.5, 25, 50, 100 μg/mL) to HeLa and WI-38, respectively. As shown in Fig. S20 (Supporting information), after co-incubation of HeLa and WI-38 cells with concentration-dependent **Gd_9** solution for 16 h, the cell survival rate exceeded 75%, demonstrating that **Gd_9** has low cytotoxicity (Fig S20 in Supporting information). At the same time, **Gd_9** (100 μg/mL, 50 μL/healthy mice) was injected into healthy mice through the tail vein for 48 h, followed by routine blood tests and pathological analysis of H&E staining of major organs. The results of *in vivo* safety evaluation showed that **Gd_9** showed excellent biocompatibility (Figs. S21 and S22). Obviously, high-nuclear gadolinium clusters that highly cluster Gd(III) at the molecular level have more attractive prospects in MRI CAs. Therefore, it is crucial to construct high-nuclear gadolinium clusters that are stable and suitable in aqueous solutions for application as novel CAs for MRI.

In summary, the chelating ligand protection strategy was used to synthesize nonanuclear lanthanide nanoclusters **Ln_9** that are stable in aqueous solution under solvothermal "one-pot" conditions. The nanosized nonanuclear **Eu_9** still shows bright characteristic red emission of Eu(III) ions in aqueous solution and can show excellent fluorescence imaging performance for many different types of cells. Notably, the cationic **Eu_9** nanocluster can specifically target and label mitochondria in cells. To our knowledge, this is the first time that the cationic properties of lanthanide nanoclusters have been used to achieve specific fluorescence labeling of mitochondria. In addition, nonanuclear **Eu_9** can also be taken up by zebrafish eggs and larvae, showing high-resolution *in vivo* imaging. The longitudinal and transverse relaxation rates r_1 and r_2 of the nonanuclear nanocluster **Gd_9** with highly aggregated Gd(III) ions are 39.42 and 50.58 mmol L^{-1} s^{-1}, respectively, showing great potential as an excellent T_1-weighted MRI CA. This work not only opens a door for the application of lanthanide nanocluster emitters in the field of organelle imaging, but also has the potential to develop multimodal imaging applications based on lanthanide nanocluster emitters.

CRediT authorship contribution statement

Meng-Juan Tang: Writing – original draft, Visualization, Software, Methodology, Investigation, Formal analysis, Data curation. **Zhong-Hong Zhu:** Writing – review & editing, Supervision, Methodology, Investigation. **Hai-Ling Wang:** Writing – review & editing, Writing – original draft, Visualization, Validation, Project administration, Methodology, Investigation, Funding acquisition, Conceptualization. **Fu-Pei Liang:** Visualization, Supervision, Methodology, Funding acquisition. **Hua-Hong Zou:** Writing – review & editing, Visualization, Project administration, Investigation, Funding acquisition, Formal analysis, Conceptualization.

Declaration of competing interest

The authors declare that they have no known competing financial interests or personal relationships that could have appeared to influence the work reported in this paper.

Acknowledgments

This work was supported by the Natural Science Foundation of Guangxi (No. 2025GXNSFDA069029), the National Natural Science Foundation of China (No. 22271068), the Startup Fund of Guangxi University (No. ZX1080030424008), and Innovation Project of Guangxi Graduate Education (No. YCSW2025169).

Supplementary materials

Supplementary material associated with this article can be found, in the online version, at doi:10.1016/j.cclet.2025.112126.

References

[1] J.H. Jia, Q.W. Li, Y.C. Chen, J.L. Liu, M.L. Tong, Coord. Chem. Rev. 378 (2019) 365–381.
[2] N. Wu, H. Zhao, Y. Lei, Chin. J. Struct. Chem. 43 (2024) 100392.
[3] X.Z. Li, C.B. Tian, Q.F. Sun, Chem. Rev. 122 (2022) 6374–6458.
[4] X.M. Luo, Y.K. Li, X.Y. Dong, S.Q. Zang, Chem. Soc. Rev. 52 (2022) 383–444.
[5] B. Lin, Y. Zhang, W. Li, et al., eScience 4 (2024) 100180.
[6] W. Huang, W. Chen, Q. Bai, et al., Angew. Chem. Int. Ed. 61 (2022) e202205385.
[7] X.Y. Li, H.F. Su, Q.W. Li, et al., Angew. Chem. Int. Ed. 58 (2019) 10184–10188.
[8] X.M. Luo, Z.B. Hu, Q.F. Lin, et al., J. Am. Chem. Soc. 140 (2018) 11219–11222.
[9] N. Xu, W. Chen, J. Miao, Y. Ding, Z. Zheng, Angew. Chem. Int. Ed. 63 (2024) e202409109.
[10] X.Y. Zheng, Y.H. Jiang, G.L. Zhuang, et al., J. Am. Chem. Soc. 139 (2017) 18178–18181.
[11] W. Huang, Q. Yang, W. Chen, Z. Zheng, J. Am. Chem. Soc. 147 (2025) 5572–5576.
[12] P. Singh, S. Kachhap, P. Singh, S.K. Singh, Coord. Chem. Rev. 472 (2022) 214795.
[13] D. Yang, H. Li, H. Li, Coord. Chem. Rev. 514 (2024) 215875.
[14] Q. Zhang, J. Hu, Q. Li, et al., Chin. Chem. Lett. 33 (2022) 1417–1421.
[15] N. Xu, W. Chen, Y.S. Ding, Z. Zheng, J. Am. Chem. Soc. 146 (2024) 9506–9511.
[16] K. Binnemans, Chem. Rev. 109 (2009) 4283–4374.
[17] S.V. Eliseeva, J.C.G. Bünzli, Chem. Soc. Rev. 39 (2010) 189–227.

[18] F. Lang, J. Pang, X.H. Bu, eScience 4 (2024) 100231.
[19] Y.L. Li, H.L. Wang, Z.H. Zhu, F.P. Liang, H.H. Zou, Coord. Chem. Rev. 493 (2023) 215322.
[20] H.L. Wang, Z.H. Zhu, H.H. Zou, Chin. J. Struct. Chem. 43 (2024) 100372.
[21] Y.L. Li, H.L. Wang, Z.H. Zhu, et al., Nat. Commun. 15 (2024) 2896.
[22] B. Yu, Z.H. Zhu, W.W. Qin, et al., ACS Mater. Lett. 6 (2024) 3312–3326.
[23] M.J. Tang, Z.H. Zhu, Y.L. Li, et al., J. Colloid Interf. Sci. 680 (2025) 235–246.
[24] P. Caravan, J.J. Ellison, T.J. McMurry, R.B. Lauffer, Chem. Rev. 99 (1999) 2293–2352.
[25] Y. Geng, T. Wu, Q. Han, et al., Chin. Chem. Lett. 34 (2023) 107685.
[26] S. Coimbra, S. Rocha, N.R. Sousa, et al., Int. J. Mol. Sci. 25 (2024) 4071.
[27] H.L. Wang, D. Liu, J.H. Jia, et al., Natl. Sci. Rev. 10 (2023) nwad036.
[28] Y.L. Yang, X.M. Hu, Z. Yang, W. Huang, Adv. Funct. Mater. 35 (2025) 2412970.
[29] Z. Wang, L. He, B. Liu, et al., J. Am. Chem. Soc. 142 (2020) 16409–16419.
[30] Z. Li, D. Wang, Z. Zhou, et al., Inorg. Chem. 61 (2022) 20814–20823.
[31] W.W. Qin, Y.L. Li, Z.H. Zhu, et al., Inorg. Chem. 63 (2024) 16740–16749.
[32] T. Wang, H. Wang, W. Sun, Cryst. Growth Des. 24 (2024) 8076–8084.
[33] G.H. Zhang, H.L. Wang, Y.L. Li, et al., Adv. Funct. Mater. 35 (2025) 2425095.
[34] W. Ma, D. Liang, Q. Qian, et al., eScience 3 (2023) 100089.
[35] H.Q. Yin, X.Y. Wang, X.B. Yin, J. Am. Chem. Soc. 141 (2019) 15166–15173.
[36] S. Wu, Y. Lin, J. Liu, et al., Adv. Funct. Mater. 28 (2018) 1707169.
[37] H.L. Wang, Y.L. Li, H.H. Zou, F.P. Liang, Z.H. Zhu, Adv. Mater. 37 (2025) 2502742.
[38] M.Y. Ye, M.X. Zhang, Q.F. Xu, et al., Sci. China Chem. 66 (2023) 1400–1405.
[39] W.W. Qin, H.L. Wang, Y.L. Li, et al., ACS Mater. Lett. 6 (2024) 4911–4921.
[40] A.R. Stram, R.M. Payne, Cell. Mol. Life Sci. 73 (2016) 4063–4073.
[41] S. Ramalho, F. Alkan, S. Prekovic, et al., Sci. Adv. 11 (2025) eadn9750.
[42] P. Aranda-martínez, J. Fernández-martínez, Y. Ramírez-casas, et al., Int. J. Mol. Sci. 23 (2022) 7348.
[43] X. Kou, Y. Cong, W.F. Dong, L. Li, Mater. Des. 240 (2024) 112855.
[44] H.L. Wang, B. Yu, F. Liang, H.H. Zou, Chin. Chem. Lett. 37 (2026) 111346.
[45] W.W. Qin, Y.L. Li, Z.H. Zhu, et al., Inorg. Chem. Front. 10 (2023) 6269–6281.
[46] Y.P. Qu, X.Da Huang, K. Xu, S.S. Bao, L.M. Zheng, Dalton Trans. 52 (2023) 10489–10498.
[47] Y. Li, F. Guo, S. Wei, et al., J. Rare Earths 42 (2024) 278–285.